HHS Public Access

Author manuscript

Nat Commun. Author manuscript; available in PMC 2014 November 14.

Published in final edited form as:

Nat Commun. ; 5: 3870. doi:10.1038/ncomms4870.

Rational strategy for shaped nanomaterial synthesis in reverse micelle reactors

Zengyan Wei and **Hiroshi Matsui***

Department of Chemistry and Biochemistry, City University of New York – Hunter College, 695 Park Ave., New York, NY 10065 (USA)

Abstract

The shape-controlled synthesis of nanoparticles was established in single-phase solutions by controlling growth directions of crystalline facets on seed nanocrystals kinetically; however, it was difficult to rationally predict and design nanoparticle shapes. Here we introduce a methodology to fabricate nanoparticles in smaller sizes by evolving shapes thermodynamically. This strategy enables a more rational approach to fabricate shaped nanoparticles by etching specific positions of atoms on facets of seed nanocrystals in reverse micelle reactors where the surface energy gradient induces desorption of atoms on specific locations on the seed surfaces. From seeds of 12 nm palladium nanocubes, the shape is evolved to concave nanocubes and finally hollow nanocages in the size ~10 nm by etching the center of {200} facets. The high surface area-to-volume ratio and the exposure of a large number of palladium atoms on ledge and kink sites of hollow nanocages are advantageous to enhance catalytic activity and recyclability.

INTRODUCTION

Previously, the evolution of the size of spherical inorganic nanoparticles (NPs) *via* atomic adsorption/desorption processes has been rationally established in one-phase solutions.[1-6] The size-dependent solubility of nanoparticles in the solution is illustrated by the Gibbs-Thomson equation[7]:

$$S_r = S_\infty \, exp\,(2\sigma V_m / rRT) \quad 1$$

where S_r and S_∞ are solubility of the nanoparticle and its bulk counterpart, σ is the specific surface energy, V_m is the molar volume of NPs, r is the particle radius, R is the gas constant, and T is the absolute temperature. In the condition of particle growth under a given precursor concentration (S_b), an equilibrium particle radius (r^*) is derived from Eq. 1[7]:

*Correspondence and requests for materials should be addressed to H.M. hmatsui@hunter.cuny.edu.

Author contributions

Z.W. and H.M. designed the research. Z.W. carried out the experiments and data analysis. H.M. supervised the research. Z.W. and H.M. wrote and edited the manuscript.

Supplementary Information is accompanies this paper at paper at http://www.nature.com/naturecommunications

Competing financial interests: The authors declare no competing financial interests.

$$r^* = \frac{2\sigma V_m}{RT\,ln(S_b/S_\infty)} \quad 2$$

To correlate the size change of NPs and ion concentration in solution for predicting the shape evolution of NPs in a typical diffusion control growth reaction, d(Δ*r*)/d*t* is derived as:

$$\frac{d\,(\Delta r)}{dt} \cong \frac{K_D\,\Delta r}{\tilde{r}^2}\left(\frac{2}{\tilde{r}} - \frac{1}{r*}\right) \quad 3$$

where Δ*r* is the standard deviation of size distribution, K_D is a constant, and $\tilde{r}$ is the mean radius of NPs.[7] From these equations, three important factors to control atomic adsorption on seed nanocrystals can be derived: 1) ion precursor concentration in solution, 2) distribution of high/low surface energy of crystalline facets on seeds, 3) topological shape of seeds. To promote the particle growth in the narrow size distribution with atomic adsorption, it is important to maintain the condition where the precursor concentration is relatively high because $r/\tilde{2}$ in Eq. 3 needs to be larger than *r** and *r** monotonically decreases with increasing S_b in Eq. 2.[1] On the contrary, etching and desorption mode of atoms from the seed nanoparticles becomes thermodynamically favorable when the precursor concentration is low (i.e., $r \tilde{<} r*$), which is the scope of this work. In addition, the surface energy is also important to determine adsorption/desorption of atoms from specific crystalline facets of seeds; when surface atoms on seed nanocrystals are exposed to solution under the minimal influence of capping agents (*i.e.*, low coverage and disorder of capping structures), desorption of atoms on high energy crystalline facets is promoted while re-adsorption could become more dominant on low energy crystalline facets, dependent upon the reactivity of desorbed species. Due to this feature, the surface energy landscape created by the distribution of facets displaying distinct surface energy can direct the shape evolution of seeds. Furthermore, the topological shape of seed nanocrystals can also affect the thermodynamic adsorption/desorption of atoms on surfaces. For example, Eq. 1 shows that the solubility of atoms from the crystalline facet is dependent on the geometric curvature of the nanoparticles (*r* in Eq. 1). It means that atoms on concave surfaces have distinct desorption property as compared to flat and convex surfaces.[8] Thus, the application of shaped nanocrystals as seeds gives one a new toolbox for designing nanoparticles in complex structures by controlling atomic adsorption/desorption in more precise patterns. And, fabricating nanoparticles in complex shapes by optimizing three factors for the shape evolution from seed nanocrystals leads to rationale pathways for designing novel nanoparticles. While polyhedron-shaped nanoparticles are dominant for the use as seeds *via* reduction of ionic precursors[9], spherical seeds delocalize the surface energy landscape and thus the shape evolution tends to be simply dependent on the distribution of crystalline faces. Since the number of displayed crystalline faces is limited on the spherical nanocrystals, it is desirable to use the faceted seed nanocrystals for more delocalized surface energy distribution if the shape needs to be rationally evolved into more complex structures through atomic adsorption/desorption.[10] Fortunately, seeds are now available in a variety of non-spherical shapes with high monodispersity due to the recent progress in shape-controlled NP synthesis.[11- 17] As explained above, the advantage for the use of non-

spherical seed nanocrystals is to add predictable surface energy gradient based on their shape. Previously, various shaped NPs were grown by adsorbing atoms on low energy facet of the seed nanocrystals in high precursor concentration.[18-30] A one-pot solvothermal method was also applied to synthesize concaved Pt nanoframes by mediating the concentration of capping agent.[31] Through the atomic adsorption approach, concaved palladium (Pd) nanocubes were also grown by adsorbing Pd atoms kinetically on {111} facets while high energy {200} facets were capped (Fig. 1-a).[32] These approaches are suitable to grow large sized NPs, but it is difficult to produce concave and hollow NPs in the size smaller than 15 nm since the size and quality of seeds limit the final dimension *via* the atomic adsorption mode.[31, 32] To fabricate smaller shaped NPs, chemical etchants were used to etch atoms on high energy facets, however the use of etchants makes the etching reaction chemistry complicated, sensitively dependent on the type of etchants and their concentration, and the interfacial dynamics of capping agents on selected crystalline facets also adds another complexity.[33-39] Previously, the shape of gold (Au) NPs was transformed from nanorods to nanospheres by desorbing capping agents by heating because atoms on the high energy surface migrate to lower surface energy facet.[40] The aspect ratio of cadmium selenide (CdSe) nanorods was also changed by transferring surface atoms to lower surface energy facets through the interparticle ripening route.[41] These strategies for nanosphere and nanorod growths inspired us to design more complex shaped NPs using the rational synthesis pathway by balancing the surface energy landscape and the topological shape of seed nanocrystals: if the seed nanocrystals display well defined surface energy distribution among crystalline facets, the resulting shape of nanocrystals after atomic desorption is predictable.

In this work, the shape of 12 nm Pd seed nanocubes is evolved to concave nanocubes and finally hollow nanocages in the size ~10 nm by etching specific positions of atoms on facets of seed nanocrystals based on the surface energy distribution in reverse micelle reactors (Fig. 1-b). The high surface area-to-volume ratio and the exposure of a large number of Pd atoms on ledge and kink sites of hollow nanocages enhance catalytic activity and recyclability in Suzuki coupling reactions.

Results

Strategy for the structural evolution from nanocube to nanocage

The etching strategy is summarized in Fig. 2-a. In step (i), the seeds of Pd nanocubes are dispersed in aqueous compartment of reverse micelle. The Pd nanocube seeds are hydrophilic as their {200} facets are protected by a well-defined bilayer of cetyltrimethylammonium bromide (CTAB) (Fig. 2-a- (i)).[24, 26, 42-44] Next, in step (ii), heating slowly evaporates water phase. In step (iii), the hydrophilic compartment becomes smaller and eventually transformed into one single layer of CTAB whose polar headgroups directly contact the well-defined bilayer of CTAB on Pd NPs, and then diffusion of the organic solvent destabilizes this capping structure. In step (iv), reduction of coverage and disorder in the packing structure of capping agents occur more dominantly at the center of {200} facets. As a result, desorption of Pd atoms from the surface of seeds is triggered due to the surface energy gradient. In addition, the formation of stable Pd complexes between

desorbed Pd atoms and CTAB in solution further promotes the release of Pd atoms and discourages the re-adsorption of Pd atoms onto the seeds. This strategy enables the localized etching of Pd atoms on the nanocube seeds, and it creates concaved nanocubes and then the shape is further evolved into nanocages as shown in Fig. 2-b.

Pd nanocubes for seeds

The Pd nanocubes were prepared in an aqueous solution at 95°C. After sodium tetrachloropalladate(II) (Na_2PdCl_4), sodium hydroxide (NaOH) and CTAB were dissolved in water and stirred vigorously at 95°C, freshly prepared ascorbic acid solution was immediately injected into the reaction system. The reaction was kept at 95°C for 30 min. The product was collected by centrifugation and washed with water. Transmission electron microscopy (TEM) image shows that as-prepared Pd nanocubes have an average size and the size distribution of 12 nm and <10%, respectively (Supplementary Fig. 1-a and 2). High-resolution TEM (HRTEM) image reveals the single crystal characteristics of the nanocubes with the lattice fringe spacing at 2.0 Å, corresponding to the {200} planes of face centered cubic (fcc) Pd (Supplementary Fig. 1-b and c). The inset in Supplementary Fig. 1-b is the indexed fast Fourier transform (FFT) pattern of Supplementary Fig. 1-b, consistent with the single crystalline pattern of the Pd nanocubes.

Generation of Pd nanocages by etching Pd nanocube seeds

The etching treatment was conducted in a reverse micelle system made of CTAB/octanol/H_2O. In 20 min after residual octanol and excess surfactants were removed by washing with ethanol and water, the edges of Pd NPs were excavated on six faces while the overall size remained the same as Pd seeds (Fig. 3-a). HRTEM image of the Pd concave nanocube in Fig. 3-b reveals darker contrasts at the corners, indicating that the sample is thicker at the corners and is thinner in between after the etching treatment. The single crystal characteristics observed along the [100] axis is demonstrated by the corresponding FFT pattern in the inset of Fig. 3-b. Fig. 3-c shows higher magnification of the corner region highlighted of a squared area in Fig. 3-b. A large number of surface atoms are situated at ledge, ledge-kink and kink sites after etching, and it generates complex lattice fringe patterns on the surface. Fig. 3-d shows the two-dimensional lattice modeling corresponding to Fig. 3-c, where a high-index {320} plane (marked in blue) composed of alternating subfacets of {110} (marked in red) and {210} (marked in black) is tentatively labeled. This result indicates that CTAB cannot completely protect these nanocrystals, and desorption of Pd atoms from the seed is predominant while the rate of re-adsorption on lower energy surfaces is negligible at this early stage of shape evolution. This sparse growth may be attributed to the low concentration of and the low reactivity of Pd species in the hydrophobic solution.

After 1 hr of further etching treatment, the concaved nanocubes were transformed into hollow nanocages (Fig. 4-a). Fig. 4-b shows TEM images of individual nanocages at different angles. The average edge length of nanocage is 10 nm, 2 nm shorter than the one for the seed (Supplementary Fig. 2). It suggests that atoms on the corners of seeds started to dissolve into the solution at this aging time. The hollow structure of Pd nanocage was also confirmed from a series of TEM images obtained through tilting the sample stage at a variety of angles (Supplementary Fig. 3). The nearly pure composition of Pd of the

nanocage was confirmed by the energy-dispersive X-ray (EDX) spectrum (Supplementary Fig. 4). While the nanocages are single-crystalline in general (Supplementary Fig. 5), some NPs show polycrystalline characteristics. As shown in the HRTEM image of Fig. 4-c and its corresponding inverse FFT images (Supplementary Fig. 6), the edges of the nanocages are imaged along [100], where the (020) and (002) planes of fcc Pd are indexed. Meanwhile, the left upper corner area of the nanocages is imaged along [1-10], and lattice fringes corresponding to (020) and (111) planes of fcc Pd are resolved. A vacancy separating these two crystalline zones is marked with an arrow in Fig. 4-c. The polycrystalline characteristics are also confirmed by the FFT pattern in the inset of Fig. 4-c, where a superposition of [100] and [1-10] zones are indexed. The observation of shape transformation from nanocubes to concave nanocubes and finally hollow nanocages indicates that the shape evolution occurs thermodynamically so that the etching patterns are consistent with surface energy landscape created by the reorganization of capping agents in the diminishing reverse micelle compartment. The observation of atomic re-adsorption on the lowest energy {111} facets[45] with complicated lattice fringes with atoms on ledge, ledge-kink and kink sites (Fig. 4-c) becomes more noticeable after 1 hr of the shape evolution, probably due to the increased concentration of Pd in solution inducing their re-adsorption on these sites.

As illustrated in Fig. 2-a, the shape evolution of seed nanocubes is driven by the structure change of capping layers on seed nanocrystals after water compartment is evaporated in the reverse micelle system. To probe the packing condition of CTAB capped on shaped nanoparticles, Fourier transform infrared (FTIR) spectroscopy is applied to Pd nanocubes before and after etching, where peak positions and widths of C-CH_2 asymmetric and symmetric stretching vibrations of the methylene chain of CTAB can be used to assess the nature of surfactant packing on solid surfaces.[40, 46] In Supplementary Fig. 7, as compared with the crystalline CTAB, both stretching vibrations shift to the higher frequency for CTAB-capped Pd nanocubes (from 2917 cm^{-1} to 2920 cm^{-1} for the asymmetric band and from 2849 cm^{-1} to 2851 cm^{-1} for the symmetric band). The lower vibrational frequency and the narrower bandwidth for the crystalline surfactant correspond to more ordered structures of the methylene chains of CTAB.[40, 46] Since the stretching bands for CTAB on Pd nanocubes are blue-shifted relative to crystalline CTAB and their frequencies are comparable to the ones on gold nanorods (2921 and 2851 cm^{-1}, respectively), CTAB forms a well-defined bilayer capped on Pd nanocubes with less degree of packing order than the crystalline state.[38] Because both symmetric and asymmetric bands for CTAB on Pd nanocages are further shifted to 2922 cm^{-1} and 2853 cm^{-1}, respectively (Supplementary Fig. 7), it indicates that CTAB covers the surface of Pd nanocages with less packing order and surface coverage as compared to Pd nanocubes, yielding a large number of less protected surface atoms exposed at ledge, ledge-kink and kink sites,[40, 46] consistent with nanoscopic structures in Fig. 4-c.

Effect of solvents on atomic desorption

In addition to the effect of the surface energy distribution, desorption of Pd atoms from the seed nanocrystals could be promoted by the formation of stable Pd complexes between desorbed Pd atoms and solute molecules. To confirm this hypothesis, we carried out UV-Vis absorption measurements of solution during the shape evolution process. In the experimental

condition, Pd atoms dissolved from {200} facets in octanol can readily oxidized into $CTA^+[PdX_4]^{2-}$ complex species (X = Cl or Br),[24, 47] and a minute amount of the oxidized forms of ascorbic acid residue (*e.g.* semidehydroascorbic acid, dehydroascorbic acid) in the Pd seed solution may serve as oxidants. After 1 hr of etching and Pd NPs were separated by centrifugation, the remained supernatant was analyzed. While octanol solution containing only CTAB (20 mg mL^{-1}) shows no absorption peaks, the spectrum of supernatant shows two peaks at 250 nm and 340 nm, respectively (Supplementary Fig. 8-a). Both peaks are corresponded to the ones for $CTA^+[PdX_4^{2-}]$ complex ions.[47] A series of UV-Vis spectra of $CTA^+[PdX_4^{2-}]$ with the concentration ranging from 0 to 54 mM in octanol also showed the similar absorption profile (Supplementary Fig. 8-b), and they follow the Beer-Lambert law as shown in Supplementary Fig. 8-c. This result suggests that the desorbed individual Pd atoms are highly reactive in solution and they can readily be oxidized and form the stable complex during the etching treatment. Since the relatively high stability of complexes between Pd atoms and solute molecules promotes the desorption of Pd atoms from Pd nanocubes, types of solvents should also influence the etching process. As shown in Supplementary Fig. 9-a, when the seeds were aged in ethylene glycol (EG), a polar solvent, instead of octanol, NPs were grown in larger sizes while maintaining their cubic shape, indicating that the bilayer capping of CTAB on {200} facets was intact. Because no obvious etching was not observed on the seed nanocrystals, the reaction rates of dissolving of small NPs and the growth of large NPs are equally high and large NPs grow at the expense of smaller seeds as seen in Ostwald ripening. The faster crystal growth in EG is attributed to the higher reactivity of $CTA^+[PdX_4]^{2-}$ in the polar solvent.[48, 49] When the reaction was conducted in a 1:1 EG/octanol solution, normal Ostwald ripening was still observed, however NPs no longer maintained their cubic shape (Supplementary Fig. 9-b). Adding octanol to EG solution increased the hydrophobicity of the solution, and it seems to destabilize the bilayer structure of CTAB on {200} facets of Pd nanocubes so that the shape of NPs became irregular after aging at elevated temperature.

Catalytic performance and mechanism

Because the hollow Pd nanocages have the large surface area-to-volume ratio and they also exhibit the high density of catalytically active atoms on the ledge, ledge-kink and kink sites, these characteristics prompted us to investigate their potential catalytic performance. To this end, the catalytic activities of 10 nm Pd nanocages and 12 nm Pd nanocubes were compared in Suzuki coupling reactions. Firstly, the coupling between phenylboronic acid ($PhB(OH)_2$) and iodobenzene was investigated in 80% ethanol aqueous solution at room temperature. As shown in Fig. 5-a, Pd nanocages show superior catalytic property that a nearly complete formation (> 90%) of C-C bond is achieved within 30 min, whereas 12 nm Pd nanocubes can only promote a conversion of ~40% under the same condition and it required 75 min to reach a steady conversion of ~80%. In Fig. 5-b, Pd nanocages also demonstrate excellent recycling performance while small loss of catalytic property is observed for Pd nanocubes after circles of the re-use. The cumulative turnover number (TON = mol of product/mol Pd) over six runs for Pd nanocages (10 μg, 0.03 mol%) is 19 000, which is 1.3 times higher than the one for the Pd nanocubes. To compare them in more difficult catalytic environment, iodobenzene is replaced by iodotoluene, an electron-neutral aryl iodide, which is less reactive in the coupling reaction.[50, 51] As shown in Fig. 5-c, the reaction catalyzed by Pd

nanocages was nearly completed (>90%) after 90 min, while Pd nanocubes could convert only less than 30% of reactants at 50°C. In this harder coupling reaction between $PhB(OH)_2$ and iodotoluene, the TON for Pd nanocages (10 μg, 0.03 mol%) remains 19 000 over six runs; however it is 4.5 times higher than the one for Pd nanocubes, and the superior recyclability for Pd nanocages over Pd nanocubes is also demonstrated (Fig. 5-d). It should be noted that no homo-coupled product was observed during the coupling between $PhB(OH)_2$ and iodotoluene, as supported by nuclear magnetic resonance (NMR) spectra (Supplementary Fig. 10).

It is unlikely that leaching Pd atoms from Pd nanocages catalyze the Suzuki coupling reaction between aryl iodide and $PhB(OH)_2$ in Fig. 5 because if Pd atoms are released from Pd nanocages as homogeneous catalysts, deformation of the shape of nanocages along with declined catalytic turnovers should be observed in the recycling process even though some of these Pd atoms are readsorbed onto the nanocage. To firmly confirm that no leaching Pd species are involved in the Suzuki-coupling reaction, the three phase test was examined in the standard condition (0.6 mmol $PhB(OH)_2$, 0.3 mmol iodobenzene or iodotoluene, 1 mmol K_2CO_3, 10 μg Pd nanocages (0.03 mol%), 5 mL 80% ethanol aqueous solution) in the presence of NovaSyn TGR resin-supported aryl iodide (**2** in Supplementary Fig. 11).[52, 53] While the quantitative recovery of biphenyl products were still achieved in the solution phase, no biphenylamide (**6** in Supplementary Fig. 11) was detected after cleavage of the resin with trifluoroacetic acid (TFA) by gas chromatography–mass spectrometry (GC–MS) and NMR (Supplementary Fig. 12 and 13). Thus, these results indicate that no free Pd atoms or Pdorganic complexes are involved in the Suzuki coupling reactions in the aqueous solution at relatively low reaction temperature, and the catalytic reactions only take place on the surface of Pd nanocages.[54] The heterogeneous catalytic nature of Pd nanocages indirectly supports the hypothesis above that the superior catalysis is related to the large number of active Pd atoms exposed on the surface.

Discussion

The dominant desorption of Pd atoms from the center of {200} facets leads to fabricate hollow NPs with concaved framework, in the size ~10 nm, less than the one for the seeds. While the overall size of individual NPs were decreased relative to seeds in this anisotropic etching treatment, the size distribution was not notably changed due to the survival of low energy facets on seeds. To turn on the atomic desorption mode for etching, the well-defined packing structures of capping agents were disordered and their coverage on NPs was reduced *via* interference with organic solvent after the aqueous compartment of reverse micelle was evaporated (Fig. 2-a-(ii) and (iii)). Consequently, the surface energy gradient was generated, which could trigger the etching on specific locations on the seed surfaces (Fig. 2-a-(iv)).

To examine whether this approach can be applicable to generate other shaped metal nanoparticles, Au nanocages were synthesized by etching Au nanocube seeds with the same method used for the synthesis of Pd nanocages. The 3D characteristics of hollowness of Au nanocages were verified with their TEM images at different tilt angles (Supplementary Fig. 14). Thus, this experiment suggests that the atomic desorption-based etching approach can

be widely applicable to fabricate a variety of shaped nanoparticles with the simple etching mechanism.

In conclusion, the seed-etching nanofabrication approach for the shape-controlled nanoparticles was designed and demonstrated. The shape evolution from the seed nanocubes to concave nanocubes and finally hollow nanocages were observed by controlling atomic desorption from specific areas of the seed surfaces. The shape evolution occurred thermodynamically, and the etching patterns were consistent with surface energy landscape created by the structure change of capping layers in reverse micelle reactors. The stability of ion complexes between desorbed Pd ions and solute molecules was also important to promote the atomic desorption mode on the seed nanocubes. The seed-etching process sheds light on the rational design of shape-controlled synthesis of NPs. In addition to the demonstration of Pd and Au nanocage fabrications in reverse micelle reactors in this work, very recently the shape evolution was applied for fabricating platinum-nickel (Pt-Ni) bimetallic nanoframes by preferentially eroding Ni atoms distributed toward the interior of polyhedral faces of seed nanocrystals *via* oxidation.[55] Therefore, the shaped nanoparticle fabrication *via* the atomic etching strategy on selected positions of seeds is versatile and it is expected to have broad impacts on a variety of nanotechnological applications. This fabrication strategy will be beneficial for a variety of areas such as catalysis[56], plasmonics[17, 57], electronics[58, 59], and biomedicine[60-62], where rational shape-controlled synthesis of NPs in size <20 nm has significant impact on their performances.[17, 45, 58, 63] For catalysis, such small complex-shaped NPs are expected to have high catalytic activity because the complex hollow structures of Pd nanocages exhibit a large number of atoms on ledge, ledge-kink and kink sites with high surface areas.[64-68]

Methods

Chemicals

Sodium tetrachloropalladate(II) (Na_2PdCl_4, 99.995%), gold(III) chloride hydrate ($HAuCl_4$, ≥49% Au basis), sodium hydroxide (NaOH, ≥98%), sodium borohydride ($NaBH_4$, ≥99%) cetyltrimethylammonium bromide (CTAB, ≥99%), ascorbic acid (≥99.0%), 1-hydroxybenzotriazole hydrate (HOBt, 99%), N,N'-diisopropylcarbodiimide (DIC, 99%), acetic anhydride (Ac_2O, 99.5%), ethanol (≥99.5%), methanol (MeOH, ≥99.5%), 1-octanol (≥99%), dichloromethane (CH_2Cl_2, ≥99.9%), ethyl acetate (EtOAc, 99.8%), tetrahydrofuran (THF, ≥99.9%), ethylene glycol (EG, ≥99%), N,N-dmethylformamide (DMF, ≥99%), pyridine (≥99.9%), iodobenzene (98%), 4-iodotoluene (≥99%); 4-iodobenzoic acid (98%), biphenyl-4-carboxamide (96%), phenylboronic acid ($PhB(OH)_2$, >98%), deuterated chloroform ($CDCl_3$, 99.8%), deuterated dimethyl sulfoxide (DMSO-d6, 99.9%), trifluoroacetic acid (TFA, ≥99.0%), potassium carbonate (K_2CO_3, ≥99.0%) and magnesium sulfate ($MgSO_4$, ≥99.5%) were all purchased from Sigma-Aldrich, and used as received without further purification except THF which was distilled to remove tutylated hydroxytoluene (BHT). NovaSyn TGR resin (0.25 mmol/g loading) was purchased from EMD Millipore. Sartorius ultrapure water (18.2 MΩ•cm) was used in all preparations.

Synthesis of Pd nanocubes

The 12 nm Pd nanocube seeds were synthesized in the modified method on the basis of report by Niu et al.[14, 43] Typically, 600 μL of 30 mM Na_2PdCl_4 solution and 200 μL of 500 mM NaOH were added to 10 mL of 12.5 mM CTAB solution under stirring. After the solution was heated at 95 °C for 10 min, 200 μL of freshly prepared 500 mM ascorbic acid solution was added. The reaction was allowed to proceed for 30 min. Then, the product was separated by centrifugation and washed with water. The as-prepared Pd seeds were stored in water at 4°C.

Synthesis of Au nanocubes

Au nanocubes were synthesized using the seed-mediated method according to Chen et al.[69] In a typical seed synthesis, a freshly prepared, ice-cold aqueous $NaBH_4$ solution (0.01 M, 0.3 mL) was added into an aqueous mixture solution composed of $HAuCl_4$ (0.01 M, 0.125 mL) and CTAB (0.1 M, 3.75 mL). The solution was mixed by rapid inversion for 2 min, and then kept at room temperature for 1 h before use. In a typical growth reaction, CTAB (0.1 M, 6.4 mL), $HAuCl_4$ (0.01 M, 0.8 mL), and ascorbic acid (0.1 M, 3.8 mL) were sequentially added into H_2O (32 mL). 20 μL of the CTAB-stabilized seed solution was diluted 10 times with water, and then added into the growth solution. The resulting solution was mixed by gentle inversion for 10 s and then left undisturbed overnight. The product was separated by centrifugation and washed with water. The as-prepared Au nanocubes were stored in water at 4°C and using as seeds for the etching experiment.

Nanoparticle etching

The seed-etching treatment was conducted under argon (Ar) to avoid oxidation of Pd into PdO. In the typical experiment, an aqueous Pd seed solution (1 mg mL^{-1}, 200 μL) was added into octanol containing CTAB (20 mg mL^{-1}, 5 mL). A clear reverse micelle system made of CTAB/octanol/H_2O was formed with stirring and ultrasonic treatment, where Pd seed NPs were dispersed in the water phase. Subsequently, the solution was heated to 105°C to evaporate water in the reverse micelles with bubbling of Ar. It should be noted that no additional etchant was added into the reaction system. A set of products in a variety of shapes with different etching time were collected by centrifugation, and washed with ethanol twice and then water three times to remove residue oil and excess surfactants. The products were stored in water at 4°C.

The etching treatment for Au nanocubes follows the similar procedure as for Pd. Specifically, an aqueous Au nanocube solution (0.2 mg mL^{-1}, 200 μL) was added into octanol containing CTAB (20 mg mL^{-1}, 5 mL). The solution was heated to 105°C to evaporate water in the reverse micelles with bubbling of Ar. After 1 h, the products were collected by centrifugation, and washed with ethanol twice and then water three times to remove residue oil and excess surfactants. The products were stored in water at 4°C.

Catalytic evaluation in Suzuki coupling reactions

Suzuki coupling reaction was performed according to procedures in previous reports.[32, 70] For the catalytic synthesis of biphenyl compounds, $PhB(OH)_2$ (73 mg, 0.6 mmol) was added to ethanol (4 mL) with iodobenzene (34 μL, 0.3 mmol) or iodotoluene (65 mg, 0.3 mmol), in

the presence of K_2CO_3 (138 mg, 1 mmol) and aqueous solutions containing Pd NPs (1 mL, 10 μg mL^{-1}, 0.03 mol%). Reactions were carried out under vigorous stirring at room temperature for iodobenzene and 50°C for iodotoluene, respectively. The biphenyl product and unreacted aryl iodides (if any) was extracted with CH_2Cl_2 (3×5 mL), while the excess $PhB(OH)_2$ and Pd NPs were remained in the aqueous layer.[64] The organic layer was then washed with saturated K_2CO_3 solution three times, and it was dried over $MgSO_4$ powders. After filtration, CH_2Cl_2 was removed through rotary evaporation. The products were dissolved in $CDCl_3$, and analyzed with ^{1}HNMR. For the reaction between iodobenzene and $PhB(OH)_2$, the percentage yield was calculated by comparing the integration of the peak at δ 7.4 ppm (biphenyl) with that at δ 7.1 ppm (unreacted iodobenzene) (Supplementary Fig. 15). For coupling of iodotoluene with $PhB(OH)_2$, the integration of the peaks at δ 7.5 ppm (4-methylbiphenyl) and δ 6.9 ppm (unreacted iodotoluene) were used to calculate the percent yield (Supplementary Fig. 10). Pd NPs from the aqueous layers was recycled by centrifugation, and then dispersed in 1 mL H_2O. To evaluate the recyclability of catalysts, the reactions were examined by mixing fresh reagents with the recycled Pd NP solutions.

Preparation of NovaSyn TGR resin-supported aryl iodide

4-iodobenzoic acid (0.149 g, 0.6 mmol), HOBt·H_2O (0.092 g, 0.6 mmol) and DIC (94 μL, 0.6 mmol) were pre-mixed in DMF (5 ml) on ice for 1 hour. Then, NovaSyn TGR resin **1** (0.48 g, 0.25 mmol/g loading) was added (Supplementary Fig. 11). The reaction was conducted under stirring overnight at room temperature. A capping solution consisting of Ac_2O (45 μL, 0.48 mmol) and pyridine (42 μL, 0.52 mmol) was added, and the reaction was allowed for an additional 30 minutes. The product, resin **2** (Supplementary Fig. 11), was separated by filtration and washed with DMF (3 × 5 mL), MeOH (3 × 5 mL), and CH_2Cl_2 (3 × 5 mL) and dried under vacuum. The resin was stored at - 20°C prior to use.

Three phase test

Suzuki coupling reactions were performed in standard condition (0.6 mmol $PhB(OH)_2$, 0.3 mmol iodobenzene or iodotoluene, 1 mmol K_2CO_3, 10 μg Pd nanocages (0.03 mol%), 5 mL 80% ethanol aqueous solution) in the presence of resin **2** (42 mg, 0.01 mmol). Reactions were carried out under vigorous stirring at room temperature for iodobenzene and 50°C for iodotoluene, respectively. After 2 hours, the resin was separated by filtration. While the conversion of iodobenzene or iodotoluene in the filtrate were analyzed as described in "Catalytic Evaluation by Suzuki Coupling Reactions", the insoluble resins were purified by washing with H_2O (3 × 2 mL), MeOH (3 × 2 mL), EtOAc (3 × 2 mL), THF (3 × 2 mL), and CH_2Cl_2 (3 × 5 mL). Here, resin **2** would convert to resin **3** if any active homogeneous catalyst appears in the solution during the coupling reaction (Supplementary Fig. 11). This conversion can be verified by analyzing the compounds after cleavage with TFA, where **5** and **6** were cleavage products of **2** and **3**, respectively (Supplementary Fig. 11). To this end, the resin was treated with 2 mL 95% v/v TFA in CH_2Cl_2 for 30 min at room temperature. The cleavage solution was filtrated and the resin was washed with CH_2Cl_2 (3 × 2 mL), EtOAc (3 × 2 mL), and THF (3 × 2 mL). The combined filtrates were evaporated. The product was dissolved in THF, and analyzed with GC-MS (Supplementary Fig. 12). In this sample, dodecane was added as an internal standard. The product was also confirmed with ^{1}HNMR after dissolving in DMSO-d6 (Supplementary Fig. 13).

Characterization

TEM images were captured on a JEM 2100 microscope (JEOL Inc.) with an acceleration voltage of 200 kV. Samples were prepared by drying 2 μL of the NP solution on carbon-coated copper grids under ambient condition. UV-Vis absorption spectra were recorded on Beckman Coulter DU 800 UV/Vis Spectrophotometer. ^{1}HNMR spectra were recorded on Bruke 500 MHz spectrometers. Chemical shifts (δ values) were reported in ppm downfield from internal tetramethylsilane (TMS).

Supplementary Material

Refer to Web version on PubMed Central for supplementary material.

Acknowledgments

All of works were supported by the U.S. Department of Energy, Office of Basic Energy Sciences, Division of Materials Sciences and Engineering under Award No. DE-FG-02-01ER45935. Hunter College infrastructure is supported by the National Institute on Minority Health and Health Disparities (NIMHD) of the National Institutes of Health (NIH) (MD007599). We are grateful to Dr. Prachi Anand for the discussion of the three phase test. Z.W. thanks Shibin Zhao (CCNY) for the assistance of GC-MS characterization. H.M. thanks Prof. Christophe Coperet (ETH) for useful discussions regarding catalytic experiments.

References

1. Peng X, Wickham J, Alivisatos AP. Kinetics of II-VI and III-V colloidal semiconductor nanocrystal growth: “gocusing” of size distributions. J Am Chem Soc. 1998; 120:5343–5344.
2. Peng X. An essay on synthetic chemistry of colloidal nanocrystals. Nano Res. 2009; 2:425– 447.
3. Daniel M-C, Astruc D. Gold nanoparticles: assembly, supramolecular chemistry, quantum-size-related properties, and applications toward biology, catalysis, and nanotechnology. Chem Rev. 2003; 104:293–346. [PubMed: 14719978]
4. Thessing J, Qian J, Chen H, Pradhan N, Peng X. Interparticle influence on size/size distribution evolution of nanocrystals. J Am Chem Soc. 2007; 129:2736–2737. [PubMed: 17302418]
5. Chen Y, Johnson E, Peng X. Formation of monodisperse and shape-controlled MnO nanocrystals in non-injection synthesis: Self-Focusing via Ripening. J Am Chem Soc. 2007; 129:10937–10947. [PubMed: 17696349]
6. Sun S, Zeng H. Size-controlled synthesis of magnetite nanoparticles. J Am Chem Soc. 2002; 124:8204–8205. [PubMed: 12105897]
7. Sugimoto T. Preparation of monodispersed colloidal particles. Adv Colloid Interface Sci. 1987; 28:65–108.
8. Lofton C, Sigmund W. Mechanisms controlling crystal habits of gold and silver colloids. Adv Funct Mater. 2005; 15:1197–1208.
9. Xiong Y, Xia Y. Shape-controlled synthesis of metal nanostructures: the case of palladium. Adv Mater. 2007; 19:3385–3391.
10. Jun YW, Choi JS, Cheon J. Shape control of semiconductor and metal oxide nanocrystals through nonhydrolytic colloidal routes. Angew Chem Int Ed. 2006; 45:3414–3439.
11. Yu L, Banerjee IA, Matsui H. Direct growth of shape-controlled nanocrystals on nanotubes via biological recognition. J Am Chem Soc. 2003; 125:14837–14840. [PubMed: 14640660]
12. Grzelczak M, Perez-Juste J, Mulvaney P, Liz-Marzan LM. Shape control in gold nanoparticle synthesis. Chem Soc Rev. 2008; 37:1783–1791. [PubMed: 18762828]
13. Tao AR, Habas S, Yang P. Shape control of colloidal metal nanocrystals. Small. 2008; 4:310–325.
14. Niu W, Zhang L, Xu G. Shape-controlled synthesis of single-crystalline palladium nanocrystals. ACS Nano. 2010; 4:1987–1996. [PubMed: 20307089]

15. Chiu CY, Li Y, Ruan L, Ye X, Murray CB, Huang Y. Platinum nanocrystals selectively shaped using facet-specific peptide sequences. Nat Chem. 2011; 3:393–399. [PubMed: 21505499]
16. Zhang H, Jin M, Xiong Y, Lim B, Xia Y. Shape-controlled synthesis of Pd nanocrystals and their catalytic applications. Acc Chem Res. 2012
17. Xia Y, Xia X, Wang Y, Xie S. Shape-controlled synthesis of metal nanocrystals. MRS Bull. 2013; 38:335–344.
18. Cha JN, Stucky GD, Morse DE, Deming TJ. Biomimetic synthesis of ordered silica structures mediated by block copolypeptides. Nature. 2000; 403:289–292. [PubMed: 10659843]
19. Jana NR, Gearheart L, Murphy CJ. Seeding growth for size control of 5–40 nm diameter gold nanoparticles. Langmuir. 2001; 17:6782–6786.
20. Jana NR, Gearheart L, Murphy CJ. Wet chemical synthesis of high aspect ratio cylindrical gold nanorods. J Phys Chem B. 2001; 105:4065–4067.
21. Jana NR, Gearheart L, Murphy CJ. Seed-mediated growth approach for shapecontrolled synthesis of spheroidal and rod-like gold nanoparticles using a surfactant template. Adv Mater. 2001; 13:1389–1393.
22. Aizenberg J, Muller DA, Grazul JL, Hamann DR. Direct fabrication of large micropatterned single crystals. Science. 2003; 299:1205–1208. [PubMed: 12595685]
23. Nikoobakht B, El-Sayed MA. Preparation and growth mechanism of gold nanorods (NRs) using seed-mediated growth method. Chem Mater. 2003; 15:1957–1962.
24. Sun Y, et al. Seedless and templateless synthesis of rectangular palladium nanoparticles. Chem Mater. 2007; 19:2065–2070.
25. Dickerson MB, Sandhage KH, Naik RR. Protein- and peptide-directed syntheses of inorganic materials. Chem Rev. 2008; 108:4935–4978. [PubMed: 18973389]
26. Chen Y-H, Hung H-H, Huang MH. Seed-mediated synthesis of palladium nanorods and branched nanocrystals and their use as recyclable suzuki coupling reaction catalysts. J Am Chem Soc. 2009; 131:9114–9121. [PubMed: 19507854]
27. Sommerdijk NAJM, Cölfen H. Lessons from nature—biomimetic approaches to minerals with complex structures. MRS Bull. 2010; 35:116–121.
28. Kim YY, et al. An artificial biomineral formed by incorporation of copolymer micelles in calcite crystals. Nat Mater. 2011; 10:890–896. [PubMed: 21892179]
29. Li H, Kanaras AG, Manna L. Colloidal branched semiconductor nanocrystals: state of the art and perspectives. Acc Chem Res. 2013; 46:1387–1396. [PubMed: 23369428]
30. Qi Y, et al. Kinetically controlled synthesis of Pt-Cu alloy concave nanocubes with high-index facets for methanol electro-oxidation. Chem Commun. 2014; 50:560–562.
31. Xia BY, Wu HB, Wang X, Lou XW. Highly concave platinum nanoframes with high-index facets and enhanced electrocatalytic properties. Angew Chem Int Ed. 2013; 52:12337– 12340.
32. Jin M, Zhang H, Xie Z, Xia Y. Palladium concave nanocubes with high-index facets and their enhanced catalytic properties. Angew Chem Int Ed. 2011; 50:7850–7854.
33. Zhang H, Jin M, Xia Y. Noble-metal nanocrystals with concave surfaces: synthesis and applications. Angew Chem Int Ed. 2012; 51:7656–7673.
34. Mulvihill MJ, Ling XY, Henzie J, Yang P. Anisotropic etching of silver nanoparticles for plasmonic structures capable of single-particle SERS. J Am Chem Soc. 2009; 132:268– 274. [PubMed: 20000421]
35. Cheong S, Watt J, Ingham B, Toney MF, Tilley RD. In situ and ex situ studies of platinum nanocrystals: growth and evolution in solution. J Am Chem Soc. 2009; 131:14590– 14595. [PubMed: 19754052]
36. Ren J, Tilley RD. Preparation, Self-assembly, and mechanistic study of highly monodispersed nanocubes. J Am Chem Soc. 2007; 129:3287–3291. [PubMed: 17311381]
37. Chen Y, Chen Q-S, Peng S-Y, Wang Z-Q, Lu G, Guo G-C. Manipulating the concavity of rhodium nanocubes enclosed by high-index facets via site-selective etching. Chem Commun. 2014; 50:1662–1664.
38. Zheng Y, Zeng J, Ruditskiy A, Liu M, Xia Y. Oxidative etching and its role in manipulating the nucleation and growth of noble-metal nanocrystals. Chem Mater. 2013; 26:22–33.

39. Xie S, Lu N, Xie Z, Wang J, Kim MJ, Xia Y. Synthesis of Pd-Rh core–frame concave nanocubes and their conversion to Rh cubic nanoframes by selective etching of the Pd cores. Angew Chem Int Ed. 2012; 51:10266–10270.
40. Nikoobakht B, El-Sayed MA. Evidence for bilayer assembly of cationic surfactants on the surface of gold nanorods. Langmuir. 2001; 17:6368–6374.
41. Peng ZA, Peng X. Mechanisms of the shape evolution of CdSe nanocrystals. J Am Chem Soc. 2001; 123:1389–1395.
42. Wang F, Cheng S, Bao Z, Wang J. Anisotropic overgrowth of metal heterostructures induced by a site-selective silica coating. Angew Chem Int Ed. 2013; 52:10344–10348.
43. Niu W, et al. Seed-mediated growth of nearly monodisperse palladium nanocubes with controllable sizes. Cryst Growth Des. 2008; 8:4440–4444.
44. Shen XS, Wang GZ, Hong X, Zhu W. Simple-cubic microcubes assembled by palladium nanocubes. CrystEngComm. 2009; 11:753–755.
45. Xia Y, Xiong Y, Lim B, Skrabalak SE. Shape-controlled synthesis of metal nanocrystals: simple chemistry meets complex physics? Angew Chem Int Ed. 2009; 48:60– 103.
46. Kung KHS, Hayes KF. Fourier transform infrared spectroscopic study of the adsorption of cetyltrimethylammonium bromide and cetylpyridinium chloride on silica. Langmuir. 1993; 9:263–267.
47. Yang C-W, Chanda K, Lin P-H, Wang Y-N, Liao C-W, Huang M-H. Fabrication of Au–Pd core–shell heterostructures with systematic shape evolution using octahedral nanocrystal cores and their catalytic activity. J Am Chem Soc. 2011; 133:19993–20000. [PubMed: 22091631]
48. Chang G, Oyama M, Hirao K. Facile synthesis of monodisperse palladium nanocubes and the characteristics of self-assembly. Acta Mater. 2007; 55:3453–3456.
49. Xiong Y, Cai H, Wiley BJ, Wang J, Kim MJ, Xia Y. Synthesis and mechanistic study of palladium nanobars and nanorods. J Am Chem Soc. 2007; 129:3665–3675. [PubMed: 17335211]
50. LeBlond CR, Andrews AT, Sun Y, Sowa JR. Activation of aryl chlorides for Suzuki cross-coupling by ligandless, heterogeneous palladium. Org Lett. 2001; 3:1555–1557.
51. Littke AF, Fu GC. A convenient and general method for Pd-catalyzed Suzuki cross-couplings of aryl chlorides and arylboronic acids. Angew Chem Int Ed. 1998; 37:3387–3388.
52. Broadwater SJ, McQuade DT. Investigating PdEnCat catalysis. J Org Chem. 2006; 71:2131–2134. [PubMed: 16497002]
53. Davies IW, Matty L, Hughes DL, Reider PJ. Are heterogeneous catalysts precursors to homogeneous catalysts? J Am Chem Soc. 2001; 123:10139–10140. [PubMed: 11592910]
54. Narayanan R, El-Sayed MA. FTIR study of the mode of binding of the reactants on the Pd nanoparticle surface during the catalysis of the Suzuki reaction. J Phys Chem B. 2005; 109:4357–4360. [PubMed: 16851502]
55. Chen C, et al. Highly crystalline multimetallic nanoframes with three-dimensional electrocatalytic surfaces. Science. 2014; 343:1339–1343. [PubMed: 24578531]
56. Macdonald JE, Bar Sadan M, Houben L, Popov I, Banin U. Hybrid nanoscale inorganic cages. Nat Mater. 2010; 9:810–815. [PubMed: 20852616]
57. Rodríguez-Lorenzo L, de la Rica R, Álvarez-Puebla RA, Liz-Marzán LM, Stevens MM. Plasmonic nanosensors with inverse sensitivity by means of enzyme-guided crystal growth. Nat Mater. 2012; 11:604–607. [PubMed: 22635043]
58. Padilha LA, et al. Carrier multiplication in semiconductor nanocrystals: influence of size, shape, and composition. Acc Chem Res. 2013; 46:1261–1269. [PubMed: 23530867]
59. Li H, et al. Synthesis of uniform disk-shaped copper telluride nanocrystals and cation exchange to cadmium telluride quantum disks with stable red emission. J Am Chem Soc. 2013; 135:12270–12278. [PubMed: 23865842]
60. Walsh D, Arcelli L, Ikoma T, Tanaka J, Mann S. Dextran templating for the synthesis of metallic and metal oxide sponges. Nat Mater. 2003; 2:386–390. [PubMed: 12764358]
61. Alkilany AM, Lohse SE, Murphy CJ. The gold standard: gold nanoparticle libraries to understand the nano–bio interface. Acc Chem Res. 2012; 46:650–661. [PubMed: 22732239]

62. Lee N, Hyeon T. Designed synthesis of uniformly sized iron oxide nanoparticles for efficient magnetic resonance imaging contrast agents. Chem Soc Rev. 2012; 41:2575–2589. [PubMed: 22138852]

63. Oh MH, et al. Galvanic replacement reactions in metal oxide nanocrystals. Science. 2013; 340:964–968. [PubMed: 23704569]

64. Mohanty A, Garg N, Jin R. A universal approach to the synthesis of noble metal nanodendrites and their catalytic properties. Angew Chem Int Ed. 2010; 49:4962–4966.

65. Cao, G. Nanostructures & nanomaterials synthesis, properties & applications. Imperial College Press; 2004.

66. Huang X, et al. Palladium-based nanostructures with highly porous features and perpendicular pore channels as enhanced organic catalysts. Angew Chem Int Ed. 2013; 52:2520–2524.

67. Fihri A, Bouhrara M, Nekoueishahraki B, Basset J-M, Polshettiwar V. Nanocatalysts for Suzuki cross-coupling reactions. Chem Soc Rev. 2011; 40:5181–5203. [PubMed: 21804997]

68. Pacardo DB, Sethi M, Jones SE, Naik RR, Knecht MR. Biomimetic synthesis of Pd nanocatalysts for the stille coupling reaction. ACS Nano. 2009; 3:1288–1296. [PubMed: 19422199]

69. Chen H, Kou X, Yang Z, Ni W, Wang J. Shape- and size-dependent refractive index sensitivity of gold nanoparticles. Langmuir. 2008; 24:5233–5237. [PubMed: 18435552]

70. Wang F, et al. Heteroepitaxial growth of high-index-faceted palladium nanoshells and their catalytic performance. J Am Chem Soc. 2010; 133:1106–1111. [PubMed: 21174411]

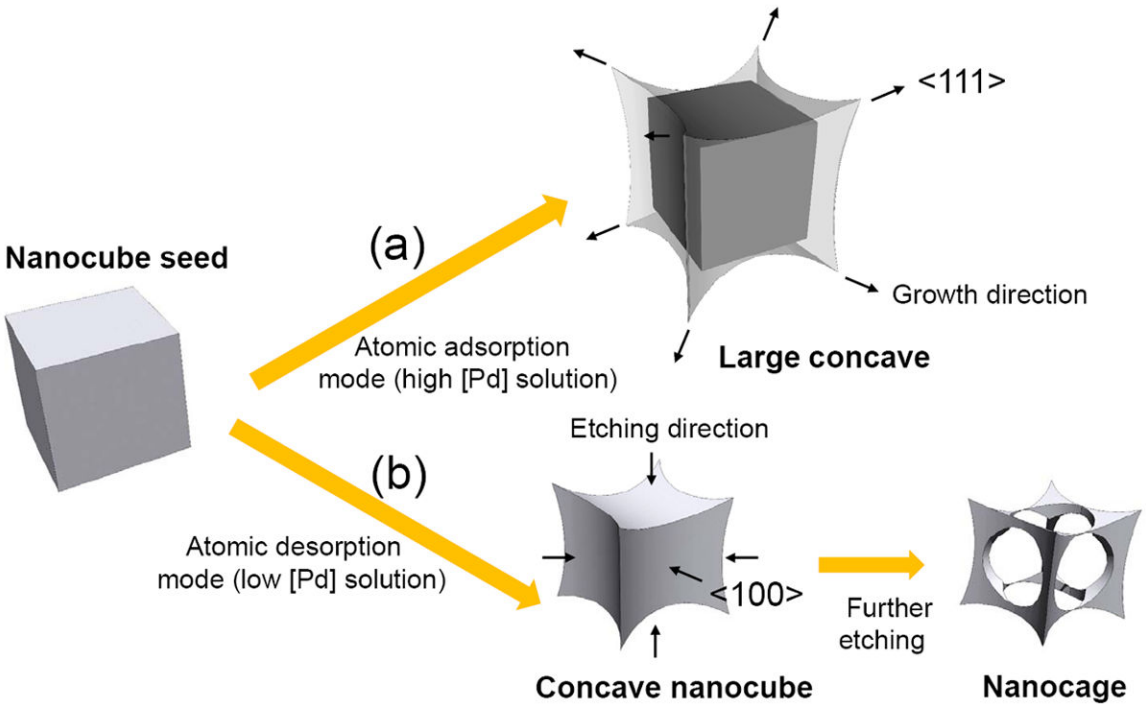

Figure 1. Shape evolution mechanisms

Evolution processes of nanocubes into the concaved shape *via* (**a**) a traditional growth approach with atomic adsorption on selected facets (**b**) an approach in this work with atomic desorption on selected facets.

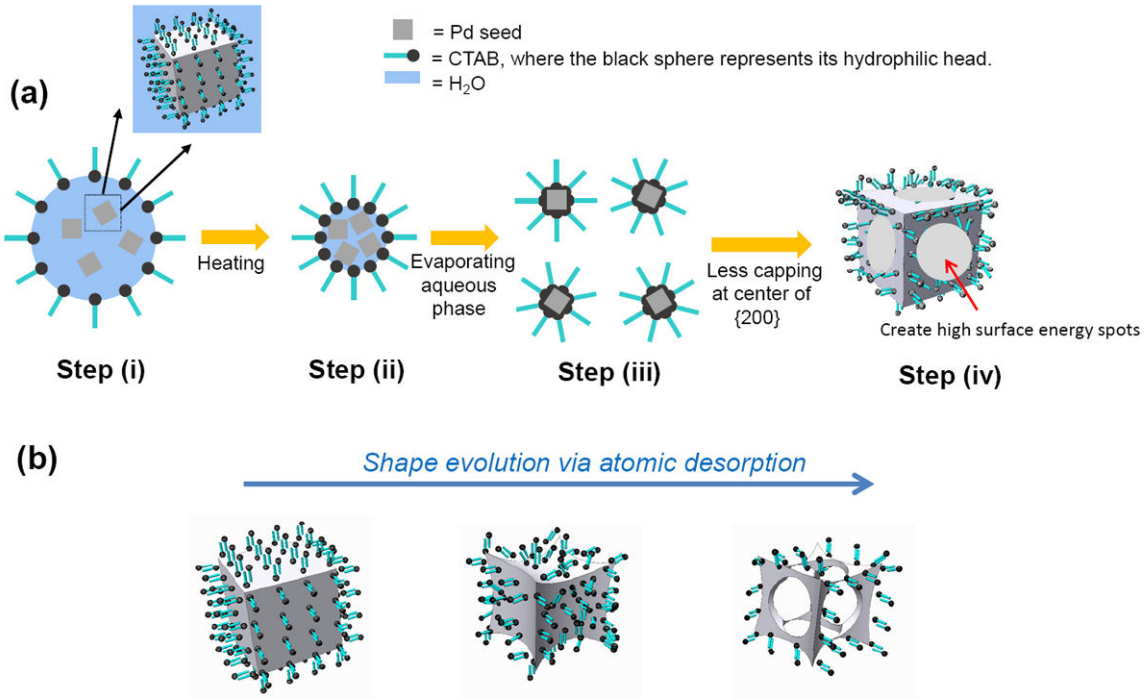

Figure 2. Shape evolution processes of seed nanocrystals in reverse micelle reactors

(**a**) Scheme for the shape evolution of Pd NPs. Step (**i**): Seeds of Pd nanocubes are dispersed in aqueous compartment of reverse micelle. Step (**ii**): Slow evaporation of water phase. Step (**iii**): Diminishing water phase induces partially removal of capping agents in octanol. Step (**iv**): Gradients of surface energy on shaped seed nanocrystals with localized capping lead to atomic desorption at high surface energy area on the seed NPs. (**b**) The etching of seed nanocubes takes place at the center of {200} facets due to the surface energy landscape in the step (**iv**). The evolution of shapes follows from concave nanocubes to nanocages with etching time.

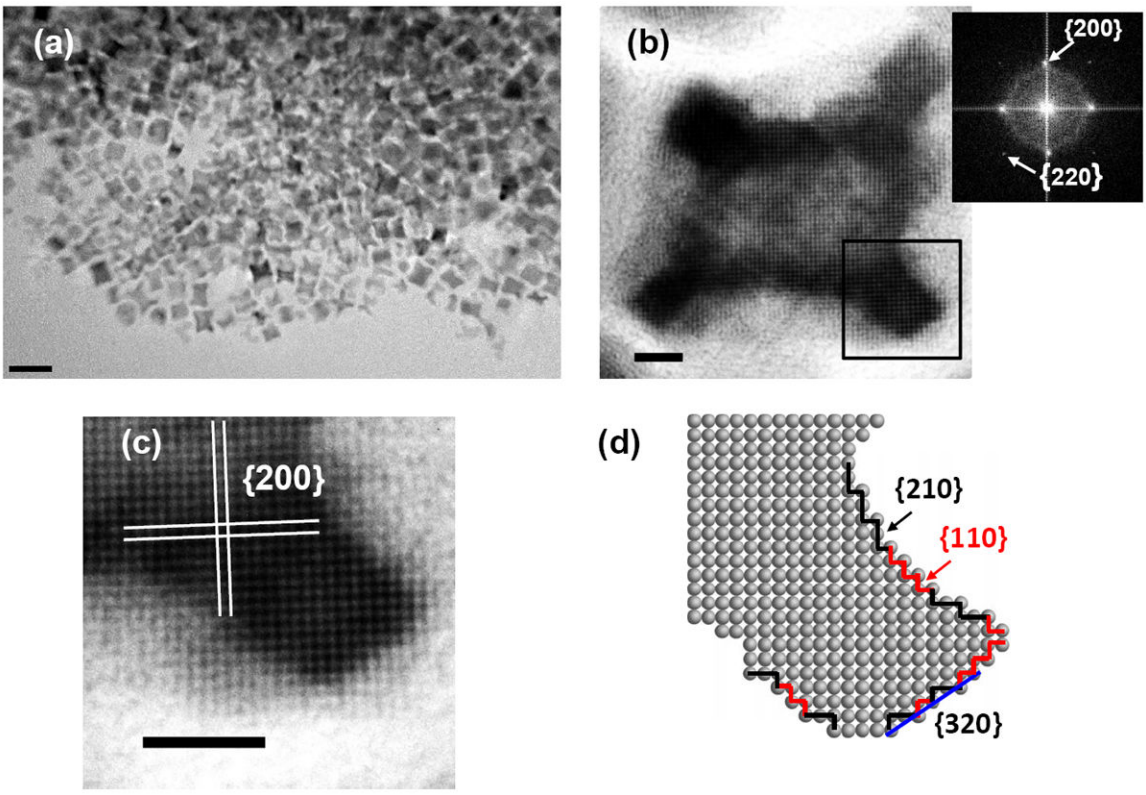

Figure 3. Structural analysis of Pd nanoconcave crystals

(**a**) TEM and (**b**) HRTEM image of the Pd concave nanocubes fabricated after 20 min of etching (inset: the FFT pattern). Scale bar = 20 nm in (**a**) and 2 nm in (**b**), respectively. (**c**) Magnified image of the square region highlighted in (**b**). Scale bar = 2 nm. (**d**) Atomic modeling corresponding to the region in (**c**), where the {110} and {210} subfacets are marked with red and black, respectively. A high-index {320} plane that is composed of alternating {110} and {210} is labeled with blue.

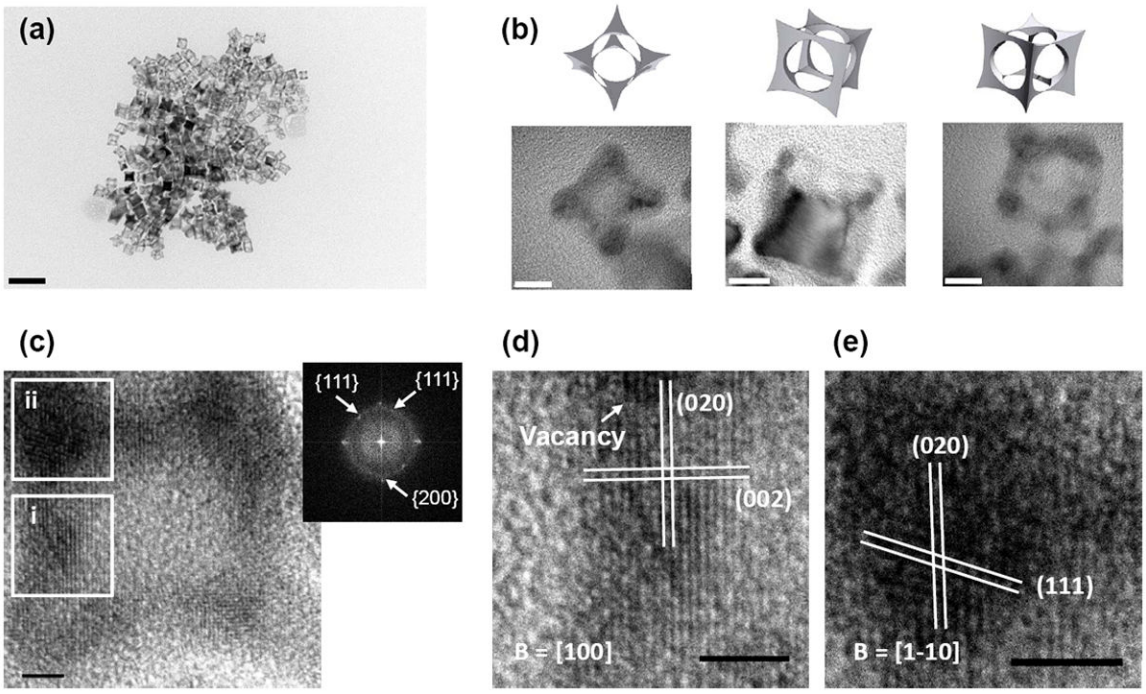

Figure 4. Structural analysis of Pd nanocages

(**a**) A low magnification TEM image to show the overall morphology of the products. Pd nanocages were generated after 1 hr of etching. Scale bar = 50 nm. (**b**) High magnification TEM images of individual nanocages in various angles. Scale bars = 5 nm. (**c**) A HRTEM image of the nanocage (inset: the FFT pattern). (**d**) A magnified image of the edge region highlighted with a blue square in (**c**). (**e**) A magnified image of the corner region highlighted with a red square in (**c**). B denotes the beam direction. Scale bars = 2 nm in (**c**) – (**e**).

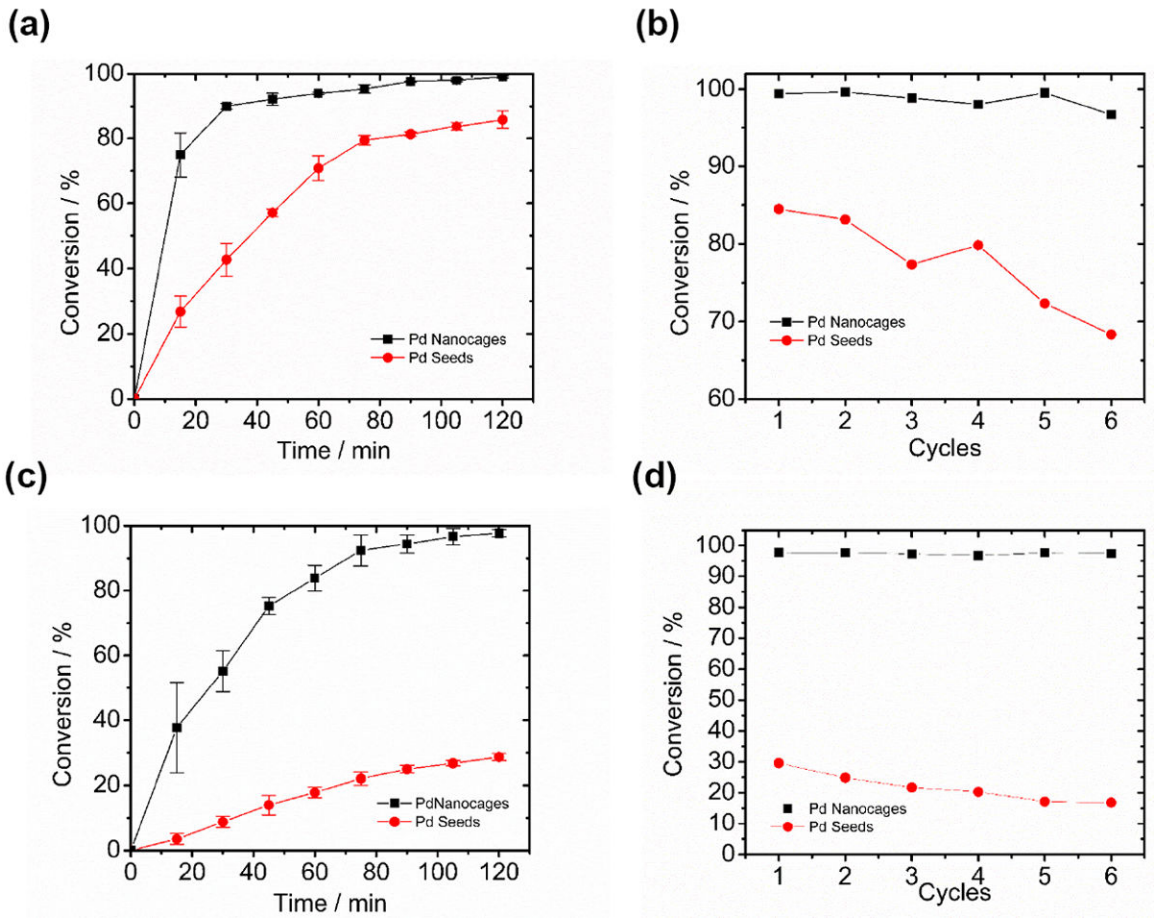

Figure 5. Catalytic performance of the Pd NPs in Suzuki coupling reaction

For the coupling reaction between phenylboronic acid and iodobenzene at room temperature: (**a**) Catalytic conversion % by 12 nm Pd nanocubes and 10 nm Pd nanocages, respectively. (**b**) Comparison of recyclability between the Pd nanocube catalyst and the Pd nanocage catalyst. For the coupling reaction between phenylboronic acid and iodotoluene at 50°C: (**c**) Catalytic conversion % by 12 nm Pd nanocubes and 10 nm Pd nanocages, respectively. (**d**) Comparison of recyclability between the Pd nanocube catalyst and the Pd nanocage catalyst. The reaction time is 120 min. In (**a**) and (**c**), error bars represent the s.d. (n = 3).